Updating the Jovian Proton Radiation Environment—2015

Henry Garrett
Luz Maria Martinez-Sierra
Jet Propulsion Laboratory

Robin Evans
Mori Associates, Inc.
Rockville, Maryland

Acknowledgments

Table of Contents

Figures

Tables

Abstract

Since publication in 1983 by N. Divine and H. Garrett, the Jet Propulsion Laboratory's plasma and radiation models have been the design standard for NASA's missions to Jupiter. These models consist of representations of the cold plasma and electrons, the warm and auroral electrons and protons, and the radiation environment (electron, proton, and heavy ions). To date, however, the high-energy proton model has been limited to an L-shell of 12. With the requirement to compute the effects of the high energy protons and other heavy ions on the proposed Europa mission, the extension of the high energy proton model from ~12 L to ~50 L has become necessary. In particular, a model of the proton environment over that range is required to estimate radiation effects on the solar arrays for the mission. This study describes both the steps taken to extend the original Divine proton model out to an L~50 and the resulting model developed to accomplish that goal. In addition to hydrogen, the oxygen, sulfur, and helium heavy ion environments have also been added between L~6 and ~50. Finally, selected examples of the model's predictions are presented to illustrate the uses of the tool.

1.   Introduction

Since their first publication in 1983 by N. Divine and H. Garrett, the Jet Propulsion Laboratory's plasma and radiation models have been the design standard for NASA's missions to Jupiter [Divine and Garrett, 1983; Garrett et al., 2015; Garrett et al., 2003; Garrett et al., 2012b; Garrett et al., 2005]. These models consist of representations of the cold plasma and electrons (~1 eV to 1 keV), the warm and auroral electrons and protons (~1 keV to 100 keV), and the radiation environment (electrons and protons from ~100 keV to 10's of MeV). Here we will describe the steps taken to extend the original high energy proton model from an L-shell of ~12 to ~50, which is required for estimating radiation effects on solar arrays for the proposed Europa mission.

By way of background, the JPL jovian environment models defined in the original Divine and Garrett model (referred to here as DG1) have been undergoing extensive revision over the last decade and were modified to improve their coverage in several earlier studies. First, the inner electron radiation belt was modified to incorporate the latest synchrotron data [Garrett et al., 2005] and a new magnetic field model VIP4 [Connerney et al., 1998] was incorporated. The region from ~8 to 50 Rj was then updated using the Galileo energetic particle detector (EPD) data [Garrett et al., 2012b]. This took the form of 1) a major revision to the plasma sheet magnetic field which is used to order the energetic particle data and 2) modification of the 8–50 Rj electron environment using the high energy Galileo EPD data. The model updates between 2003 and 2005 are collectively referred to as the Galileo Interim Radiation Electron model or GIRE. The recent 2012 update is denoted as GIRE2 (or "DG2" in this discussion). This report's revision of the proton environment specifically addresses the updating of the proton model between L 6–12 and its extension to 50 L and again uses the data from the Johns Hopkins University Applied Physics Laboratory (JHU/APL) EPD instrument on Galileo. In addition, simple models of several high energy ion components were added based on fits to the EPD measurements and will be compared with our previous studies at higher energies using the Galileo HIC (Heavy Ion Counter) experiment[Garrett et al., 2011b].

2.   The Proton Radiation Model

To repeat, the high energy proton component of the original DG1 model was limited to L values less than 12. Table A1 in Appendix A7 lists the data sets used to develop that original proton model [Divine and Garrett, 1983]. The model was based primarily on in-situ data returned by experiments on the Pioneer and Voyager spacecraft, supplemented where necessary by Earth-based radio wave observations and theoretical considerations. The DG1 model radiation belt intensity spectra at high energies include angular distributions for energetic protons inside an L-shell of 12. Major features, such as ring and satellite absorption signatures, of the magnetic field and the trapped proton distributions were modeled. Figure 1 from the original Divine and Garrett [Divine and Garrett, 1983] illustrates some of these features for the protons. Representative plots of the omnidirectional intensity versus distance along the magnetic equator, intensity versus energy, and pitch angle variations are illustrated. The detailed DG1 model is described in the Divine and Garrett paper [Divine and Garrett, 1983] and the reader is referred to that reference for the details. Here we note that the current proton model assumes the original DG1 environment predictions out to 6 L where it is joined smoothly onto the new model, which extends from 6 L to ~50 L.

To evaluate the possible effects of the protons over the Europa mission orbits, the DG2 model has been extended to ~50 L (50 Rj). To accomplish this, the Galileo EPD data from the high energy C and D detectors were reviewed for their applicability to modeling the high energy protons (E>3 MeV). The geometric factors for these high energy proton channels were estimated using the MCNPX proton transport model [Jun et al., 2002; Martinez Sierra et al., 2015; Pelowitz, 2011] and then convolved with the estimated electron and proton spectra at 9.2 Rj to determine each species' "relative" contribution to the count rate (e.g., the energy dependent fraction that the electrons or protons would contribute to the total count rate measured at 9.2 Rj). Figures 2A and 2B show the results of this process for two proton channels. Unfortunately, only one of the high energy EPD detector channels, B0, was found to be uncontaminated by electrons. This electron contamination is illustrated in Fig. 2A for the EPD DC0 14.5–33.5 MeV proton channel [Jun et al., 2002]—the relative contribution from the electrons (plot (c) in Fig. 2A) to the total count rate is estimated to be between 70% [Martinez Sierra et al., 2015] and 80% [Jun et al., 2002] at 9.2 Rj. The DC1 channel (51–59 MeV protons) is similarly contaminated with the electron contribution to the count rate approaching ~95%. In contrast, for the EPD B0 proton channel, Table 1 and Fig. 2B illustrate a "clean" channel response to protons—the channel shows no response to electrons. This channel, as originally defined by Williams et al. (1992), was intended to cover the energy range from approximately 3.2-10.1 MeV and will be used as the reference high energy proton channel in this study.
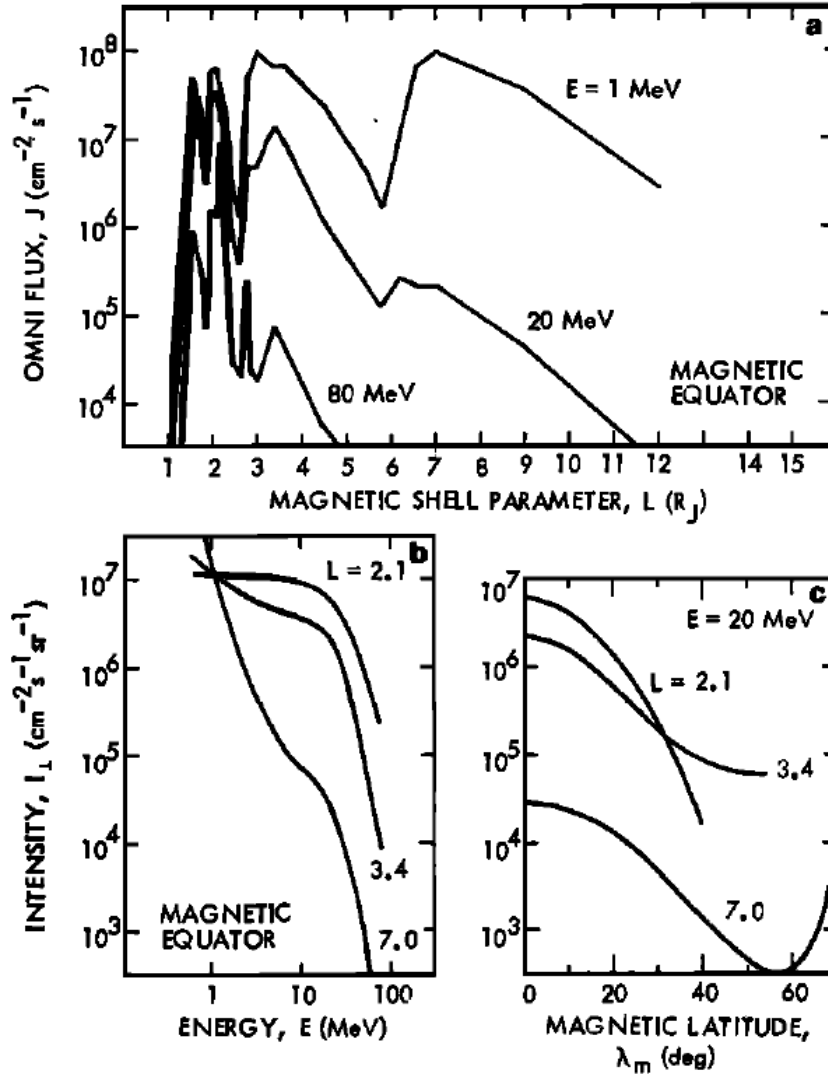
Figure 1. Sample dependences for original DG1 Jupiter energetic proton model [Divine and Garrett, 1983]. (a) Omni-directional integral flux at three energies as a function of L-shell. (b) Integral intensity at 90° pitch angle at the equator and for three L-shell values as a function of energy. (c) Integral (E > 20 MeV) intensity at 90° pitch angle for different L-shells as a function of magnetic latitude. (Note: as called out in the original caption, the increase of the intensity at L = 7 and λ_m > 55° in panel (c) was considered as a model defect associated with the fitting process.)
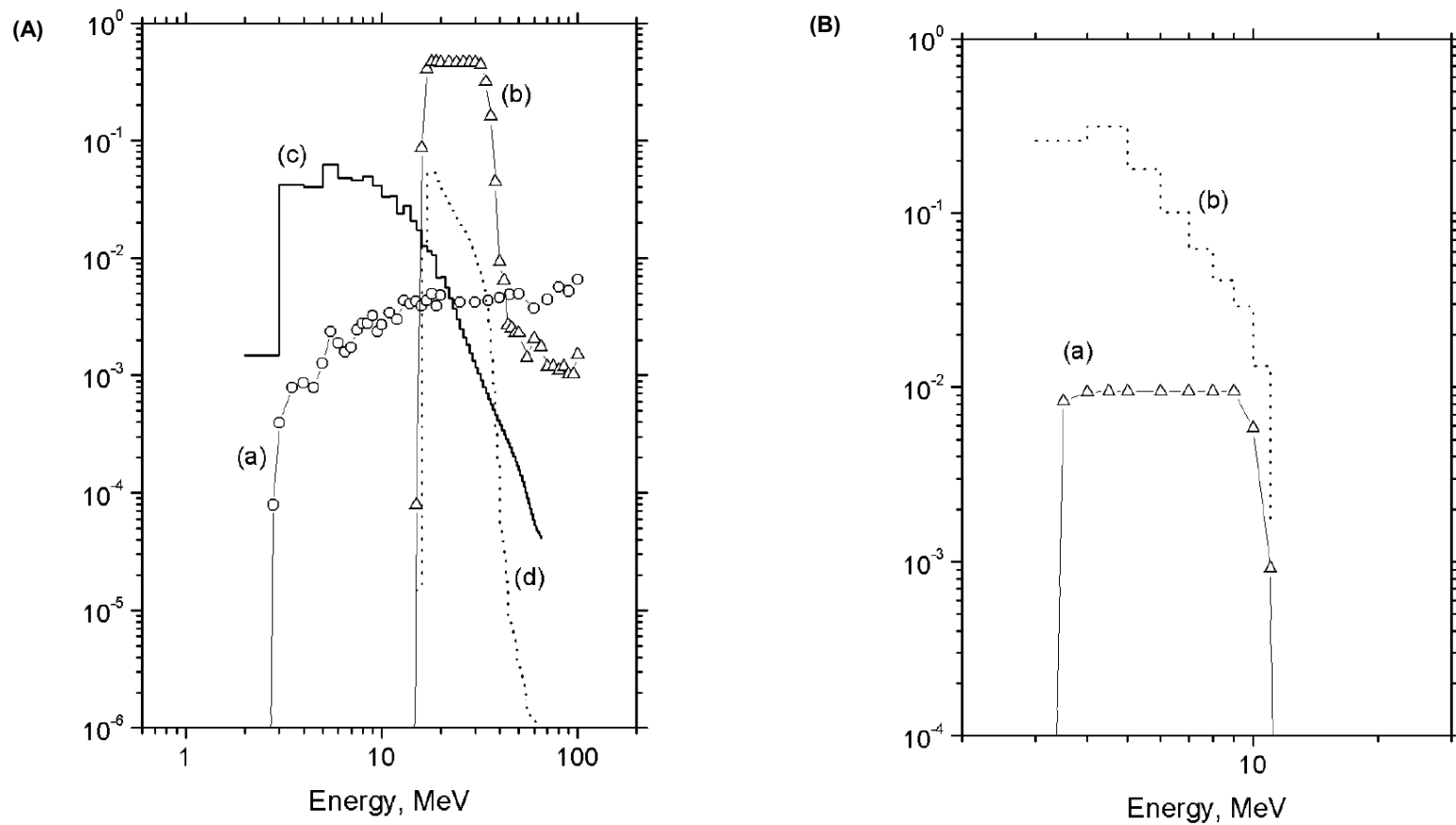
Figure 2. EPD geometric factors and relative electron and ion contributions [Jun et al., 2002]. (A) DC0 channel geometric factors and relative contributions of electrons and protons near Europa [Jun et al., 2002]: (a) electron and (b) proton geometric factors in cm²-sr versus energy; (c) electron and (d) proton relative contributions to (see text for explanation) total count rates for estimated DG1 particle fluxes at 9.2 Rj. (B) The B0 EPD channel (a) proton geometric factor in (cm²-sr) as a function of energy (see Table 1) and (b) the relative contribution of the protons, per 1 MeV energy bin, to the total count rate assuming the DG1 spectrum at 9.2 Rj [Jun et al., 2002]. The electron contribution was estimated to be zero.

Table 1. Geometric factors for the EPD B0 proton channel as estimated by the MCNPX code [Jun et al., 2002; Martinez Sierra et al., 2015].

Energy	Geometric Factor*		Geometric Factor**	
(MeV)	(cm^2-sr)	Error	(cm^2-sr)	Error
3.25	0	--	0	--
3.5	9.25E-03	7.90%	8.33E-03	8.28%
4	9.70E-03	7.70%	9.36E-03	7.81%
4.5	9.93E-03	7.60%	9.48E-03	7.76%
5	1.02E-02	7.50%	9.48E-03	7.76%
6	1.07E-02	7.30%	9.48E-03	7.76%
7	1.08E-02	7.30%	9.48E-03	7.76%
8	1.11E-02	7.20%	9.48E-03	7.76%
9	1.06E-02	7.40%	9.48E-03	7.76%
10	7.25E-03	8.90%	5.82E-03	9.90%
15	1.03E-03	23.60%	0	--
20	5.71E-04	31.60%	0	--
30	3.42E-04	40.80%	0	--
40	2.85E-04	44.70%	0	--
50	1.14E-04	70.70%	0	--
60	1.14E-04	70.70%	0	--
70	1.71E-04	57.70%	0	--
80	3.42E-04	40.80%	0	--
90	1.14E-03	22.40%	0	--
100	3.20E-03	13.40%	0	--

* Martinez Sierra et al. (2015)

**Jun et al. (2002)

Figure 3 compares various estimates of the B0 channel omnidirectional differential flux versus distance from Jupiter (R_j). These estimates are defined as follows:

1) Divine "B0": Estimates of the average omnidirectional differential flux between 3.2 and 10.1 MeV assuming the original DG1 model:

$$J(B0)_{DG1} = \frac{I(3.2\ MeV)_{DG1} - I(10.1\ MeV)_{DG1}}{10.1\ MeV - 3.2\ MeV} \qquad (1)$$

where:

$J(B0)_{DG1}$ = Differential proton intensity estimated from the DG1 model; $(cm^2$-s-MeV$)^{-1}$

$I(E)_{DG1}$ = DG1 omnidirectional integral intensity for E>3.2 MeV or E>10.1 MeV; $(cm^2$-s$)^{-1}$

2) B0(PDS): B0 channel omnidirectional differential proton fluxes estimated from 10 minute count rate averages based on the Galileo EPD data (see the NASA Planetary Data System (PDS)) between 2 to 50 Rj. The count rates were converted to differential fluxes using the following approximation:
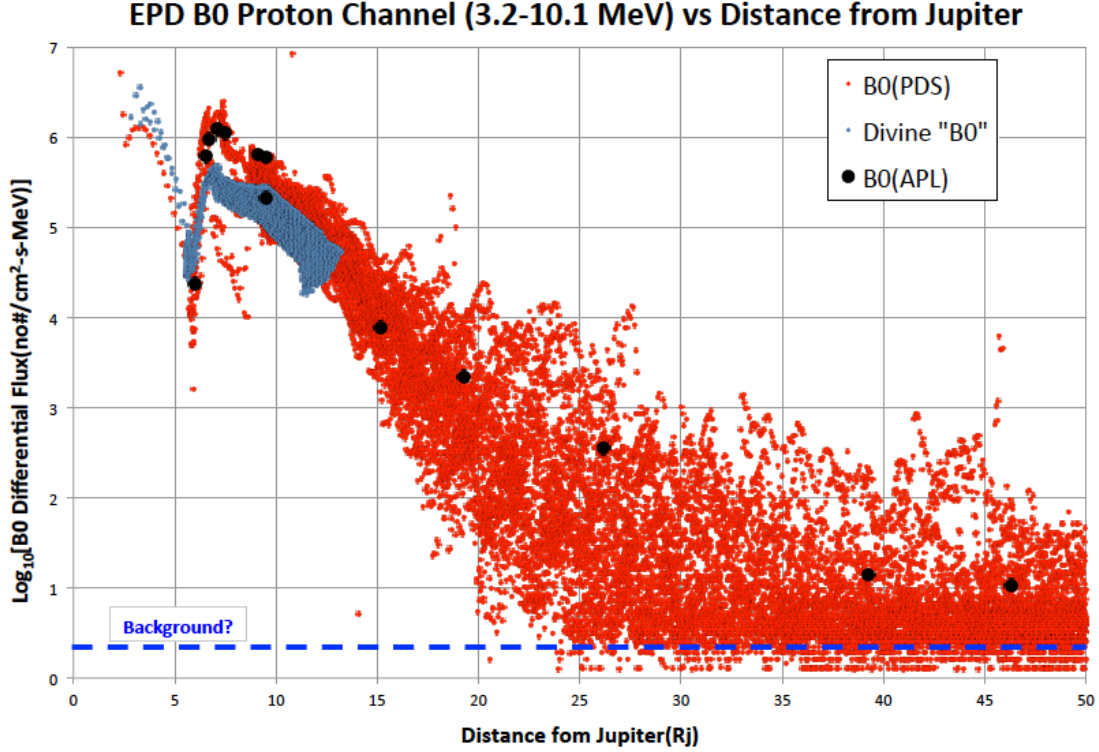
Figure 3. Scatter plot of the estimated EPD B0 differential intensity versus distance from Jupiter (Rj) for three data sources: 1) 10 minute averages of the entire Galileo EPD PDS B0 channel database (red), 2) B0 channel equivalent differential intensities for the 13 EPD reference proton spectra [Mauk et al., 2004] (black dots), and 3) the estimated 3.2–10.1 MeV proton differential intensities for the DG1 model (blue).

$$J(B0)_{PDS} = \frac{B0(Cts)\cdot 4\pi}{GF\cdot(10.1\ MeV - 3.2\ MeV)} \tag{2}$$

where:

$J(B0)_{PDS}$ = B0 channel omnidirectional differential proton flux based on observed count rates; $(cm^2\text{-s-MeV})^{-1}$

$B0(cts)$ = 10-minute averages of the B0 channel available from the PDS; (counts per second)

GF = Average Geometric Factor for B0 Channel; ~0.0094 cm^2-sr between 3.2–10.1 MeV (Table 1)

3)   B0(APL): B0 differential proton fluxes estimated from 13 published EPD proton spectra [Mauk et al., 2004] provided by APL:

$$J(B0)_{APL} = \frac{I(3.2\ MeV)_{APL} - I(10.1\ MeV)_{APL}}{10.1\ MeV - 3.2\ MeV} \tag{3}$$

where:

$J(B0)_{APL}$ = Differential proton intensity between 3.2–10.1 MeV based on published APL spectra [Mauk et al., 2004]; $(cm^2\text{-s-MeV})^{-1}$

$I(E)_{APL}$ = Omnidirectional integral intensity for energy E>3.2 MeV and E>10.1 MeV based on the integration of the APL differential spectra; $(cm^2\text{-s})^{-1}$

The third data source, again from the APL EPD instrument, is in the form of reference ion differential intensity spectra [Mauk et al., 2004] and is an important part of this study. As a first step in developing the new proton model, these differential spectra will be assumed to represent the flux distributions near the jovian magnetic equator. To determine the distributions, all the EPD ion data channels between ~50 keV to ~50 MeV were simultaneously fit by differential intensity spectra of the form given in Eq. (4) below [Mauk et al., 2004]. The fitted constants were published in tabular form and are listed in Appendix A2, Table A2, for hydrogen (and also helium, oxygen, and sulfur). Sample spectra from the APL study are plotted in Fig. 4.

$$J(E)_{APL} = C \frac{E[E_1 + kT(1+\gamma_1)]^{-1-\gamma_1}}{1+(E_1/et)^{\gamma_2}} \tag{4}$$

where:

$C, et, kT, \gamma_1, \gamma_2$ = Parameters for the APL spectral fits to the EPD data
(Mauk et al., 2004; Eq. (1))

E_1 = Energy in reference frame of moving plasma (assumed = E in this study)

The APL proton spectra as defined by Eq. (4) are next normalized to the B0 channel. That is, each proton spectrum was multiplied by the ratio of our best estimate of the B0 differential intensity as estimated along the jovian magnetic equator for the 10 minute average values to that calculated in Eq. (3) (i.e., $J(B0)_{Eq}/J(B0)_{APL}$). The derivation of the equatorial B0 intensities, $J(B0)_{Eq}$, is described next.

The B0(PDS) count rate data were analyzed to provide estimates of the proton high energy intensities on or near the magnetic equator for B0. Specifically, the B0 count rates were converted to differential intensities (fluxes) in 10 minute intervals as described by Eq. (2)—note that Eq. (2) is, in the absence of the actual particle spectrum and the detailed geometric factors of Table 1, only a rough first order approximation and will need to be justified (see later). The B0 count rates were carefully reviewed and the highest values in each ~5-hour interval were identified. These "peak" values are assumed to correspond to crossings of the Jovian magnetic equator—we note that other EPD energy channels gave somewhat different "magnetic equator" crossing times and that these all differed slightly from estimates of the magnetic equator crossings provided to us by Khurana based on the Galileo magnetometer data. Figure 5 is a plot of these "equatorial" differential fluxes for the B0 channel in terms of L-shell. The $\log_{10}$ of these B0 "equator" fluxes between 9 L and 50 L were fit, using multiple regression, with a 5th order polynomial (Eq. (5)). The six spectral fluxes (as predicted by the APL data) between 6 L and 9 L were independently fit with a separate polynomial, and the two curves joined smoothly onto each other between 8 L and 9 L. This composite curve defines a magnetic equator flux curve for B0 as a function of L between 6 L and 50 L:

Galileo APL EPD Ion Spectra at 9.13 Rj

$$J(E)_{APL} = C \frac{E[E_1 + kT(1 + \gamma_1)]^{-1-\gamma_1}}{1 + (E_1/et)^{\gamma_2}}$$

Legend:
- H+
- O+
- S+
- He+

Y-axis: Intensity (cm² s sr keV)⁻¹ — $\text{Intensity (cm}^2\text{ s sr keV)}^{-1}$
X-axis: Energy (keV)
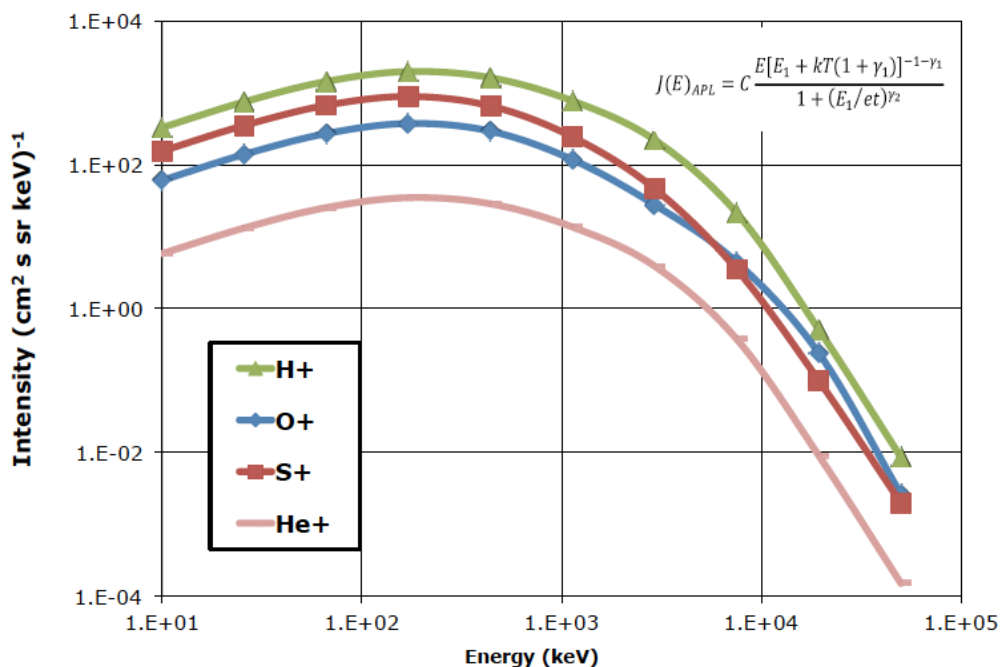
Figure 4. Sample EPD ion spectra fits (hydrogen, helium, oxygen, and sulfur) near Jupiter's equator at a radial distance of 9.13 Rj from Jupiter from the APL study [Mauk et al., 2004]. The time and position of the spectra are listed in Table A2, Appendix A2.

Magnetic Equator EPD B0 Proton Channel (3.2-10.1 MeV) vs L

Legend:
- B0 Magnetic Equator Values
- Fitted B0 Values at 13 Spectra L Values

Y-axis: $\text{Log}_{10}[\text{B0 Differential Flux(no\#/cm}^2\text{-s-MeV)}]$
X-axis: Distance from Jupiter along Magnetic Equator (L)
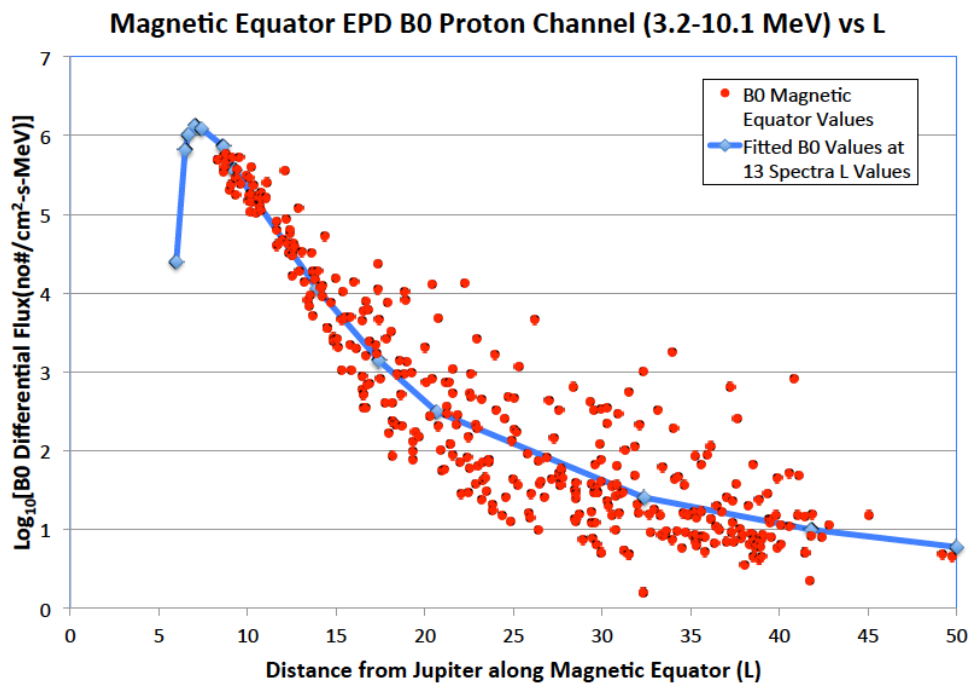
Figure 5. B0 proton channel fluxes along the magnetic equator at the indicated L locations. The blue line is the least squares fit to the $\log_{10}$ of the flux estimates as given by Eq. (5). The blue points indicate the L locations of the 13 reference proton spectra [Mauk et al., 2004].

<u>6-9 L:</u>

$$Log_{10}(J(B0)_{Eq}) = 0.0208511L^5 - 1.0117L^4 + 18.7936L^3 - 169.309L^2 + 745.499L - 1283.69$$

$$(5)$$

<u>9-50 L:</u>

$$Log_{10}(J(B0)_{Eq})$$
$$= 2.11273E-07L^5 - 2.97550E-05L^4 + 1.44131E-03L^3 - 2.30592E-02L^2$$
$$- 0.206167L + 8.51173$$

The APL reference energy spectra [Mauk et al., 2004] were multiplied by ($J(B0)_{Eq}/J(B0)_{APL}$) (where $J(B0)_{Eq}$ is given by the equatorial fluxes estimated in Eq. (5)) to give the proton spectra between 50 keV and 50 MeV at each corresponding equatorial L value. Values are provided in Table 2 (note: the APL H$^+$ spectrum for 9.49 Rj(E4 Enc) was equated to that at 9.51 Rj(E6 Enc) in our model). To obtain spectra intermediate between the L locations of the reference spectra, the log$_{10}$ fluxes between the bracketing APL spectra locations are linearly interpolated in L.

The particle fluxes drop off as one moves away from the magnetic equator. Due to the lack of data away from the magnetic equator, however, two models for this drop off are currently being considered. The first assumes that the flux is constant along an L-shell out to an L of ~62. The second assumes that the fluxes are constant along an L-shell inside L<17 but fall off exponentially with (Z_{map})^2 away from the magnetic equator beyond 22.5 L (the two regions are linearly smoothed between 17 and 22.5 L) as suggested in Hill and Michel [Hill and Michel, 1976]. That is, the differential intensity off the equator is assumed to vary as:

$$J_{B0}(L, Z_{map}) \sim B0(L)\, e^{(-(Z_{map}/H)^2)}$$

$$(6)$$

Table 2. Equatorial correction factors for the APL "C" spectrum coefficient in Eq. (4) (note: the APL H$^+$ spectrum for 9.49 Rj(E4 Enc) was equated to that at 9.51 Rj(E6 Enc) in our model).

RJ	L(VIP4)	Correction= J_{Beq}/J_{APL}	Corrected C Value
6	5.97E+00	1.044	3.09004E+05
6.52	6.47E+00	1.055	2.11069E+07
6.71	6.65E+00	1.060	8.46986E+06
7.1	7.03E+00	1.071	3.75801E+06
7.48	7.40E+00	1.082	9.67409E+09
9.13	8.63E+00	1.131	9.97843E+07
9.49	9.23E+00	1.752	7.09596E+07
9.51	9.28E+00	1.683	6.81685E+07
15.15	1.39E+01	1.460	9.98518E+10
19.28	1.74E+01	0.625	1.01888E+09
26.16	2.07E+01	0.875	1.19052E+10
39.25	3.24E+01	1.799	1.04002E+09
46.3	4.18E+01	0.919	3.08918E+08

where:

H = scale height (Rj); here assumed to vary between ~2.5–5.0 R_j

Z_{map} = distance from the magnetic equator as determined by the
Khurana and Schwarzl [2005] magnetic field model

As an example, the proton model outputs for the integral intensity E>3.2 MeV are compared to the original DG1 model in Fig. 6 for the "L-shell" model and the "Z_{map}" model for *H*=5.0 Rj. The energy range of the new model's protons (and heavy ion components) as adapted from the referenced EPD energy channels [Mauk et al., 2004] are given in Table 3.

To evaluate the new model and its variations with scale height, it will be used to predict the original B0 channel count rates (this will also allow checking the validity of Eq. (2) for converting B0 channel count rates to fluxes—see earlier remarks). This is done by convolving the predicted differential proton intensity spectrum at each 10-minute average location with the geometric factors in Table 1 [Martinez Sierra et al., 2015] over the energy range 3.25 MeV to 100 MeV and multiplying by 4π steradians. In mathematical terms:

$$(cts/s)'_{B0} = \int_{3.2 \, MeV}^{100 \, MeV} 4\pi J(E)G(E) \cdot dE \cong \sum_{i=1}^{19} 4\pi J(E_i)G(E_i) \cdot \Delta E_i \qquad (7)$$

where:

$(cts/s)''_{B0}$ = Estimated counts per second at a given location for the *B*0 channel

$J(E_i)$ = Estimated (modeled) proton differential intensity at location for energy E_i

$G(E_i)$ = Geometric factor from Table 1 for energy E_i

E_i = Energy i as listed in Table 1 (E_1=3.25 MeV, … , E_{20}=100 MeV)

$\Delta E_i = (E_{i+1} - E_i)$; $i = 1, … ,19$
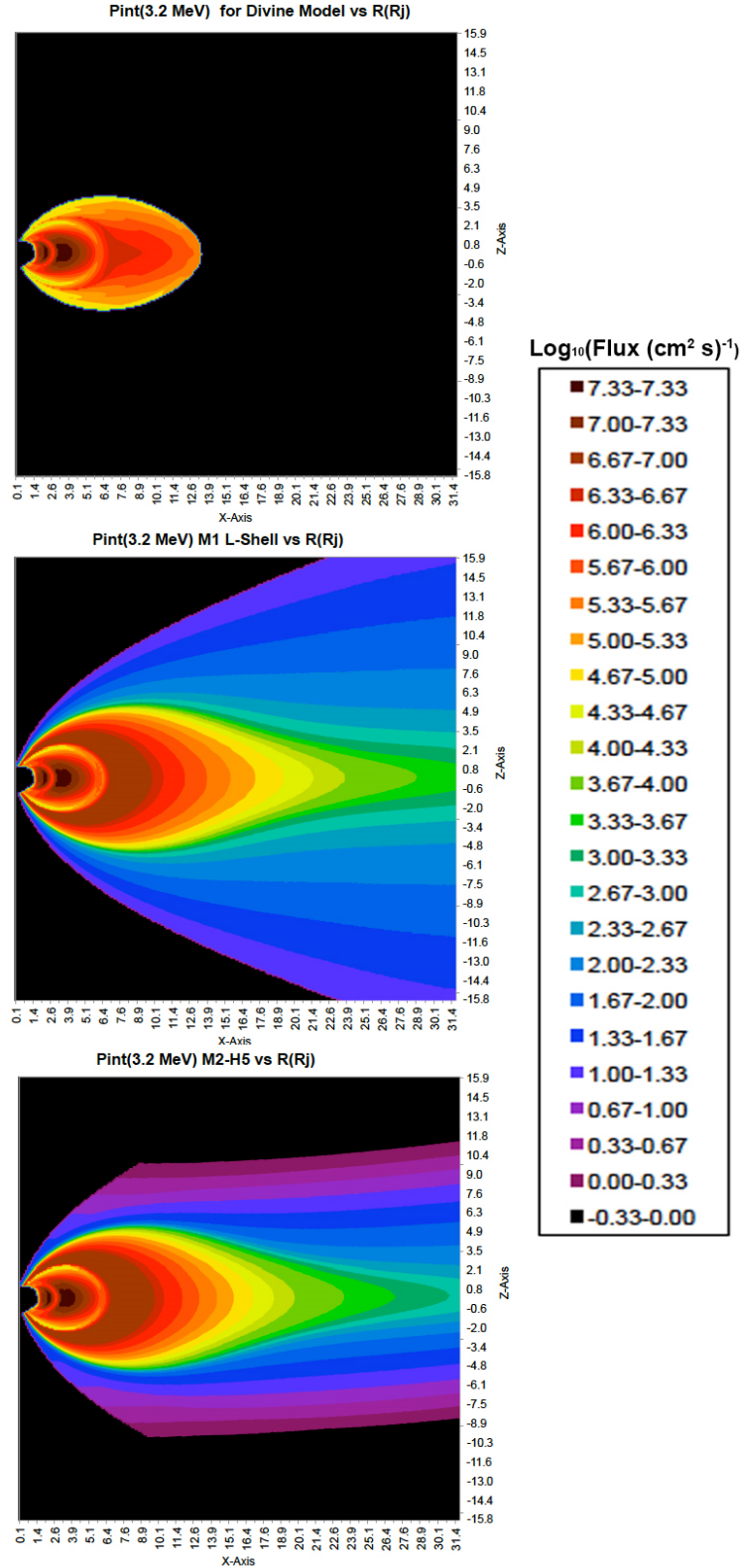
Figure 6. Comparison of the log₁₀ of the proton integral flux (E>3.2 MeV) between (top) the original (DG1) Divine-Garrett model; (middle) the new (DG2) GIRE2 model assuming that the equatorial fluxes are constant along a given L-shell; and the new GIRE2 model assuming that the fluxes fall off with a scale height of 5 Rj beyond L>17 (see text).

Table 3. Assumed ranges of validity along the magnetic equator (in Rj) and in energy of the ion components for the new DG2 proton/ion model. Values are as adapted from the 13 EPD reference ion spectra [Mauk et al., 2004].

SPECIES	ENERGY RANGE	R$_J$ RANGE
H	50 keV to 50 MeV	6–19.28
	50 keV to 32 MeV	25.16
	50 keV to 3 MeV	39.25–46.3
He	50 keV to 50 MeV	6–15.15
	50 keV to 6 MeV	19.28–25.16
	50 keV to 4 MeV	39.25–46.3
O	50 keV to 50 MeV	6–15.15
	50 keV to 18 MeV	19.28
	50 keV to 9 MeV	25.16
	50 keV to 2 MeV	39.25–46.3
S	50 keV to 50 MeV	6–15.15
	50 keV to 21 MeV	19.28
	50 keV to 10 MeV	25.16–46.3

Figure 7 compares estimates of the B0 channel count rate data versus distance (Rj) compared with the measured B0 channel counts/second (10-minute averages) between 6 L and 50 L. The actual B0 channel data are plotted along with the L-shell model assumption and two values for H (2.5 Rj and 5.0 Rj) for the scale height model. Of the three, the scale height model with H = 5.0 Rj appears to agree better qualitatively with the count rate data. Figure 8 provides a clearer picture of this rough agreement (note: some care must be taken in evaluating this graph, however, as the B0 count rate data appears to the authors to have a background count rate perhaps as high as ~0.001 to ~0.01 counts per second (cts) for the ~10-minute averaging interval as evidenced in the plot).

Similarly, Figs. 9A and 9B are direct comparisons of the B0 channel count rates with the predicted count rates for the L-shell model and the H = 5.0 Rj model. Again, the model with a scale height variation of H = 5.0 Rj appears to give a better qualitative fit. As a quantitative test, the two graphs were fit using a simple linear fit in terms of the $\log_{10}$ of the variables between L = 6 and 50. The Fig. 9A regression fit gives:

$$Log_{10}(B0(Model\ 1)) = 0.8998\ Log_{10}(B0(DATA)) + 0.1183 \qquad (8)$$

The Fig. 9B regression fit is:

$$Log_{10}(B0(Model\ 2)) = 0.9883\ Log_{10}(B0(DATA)) + 0.0811 \qquad (9)$$
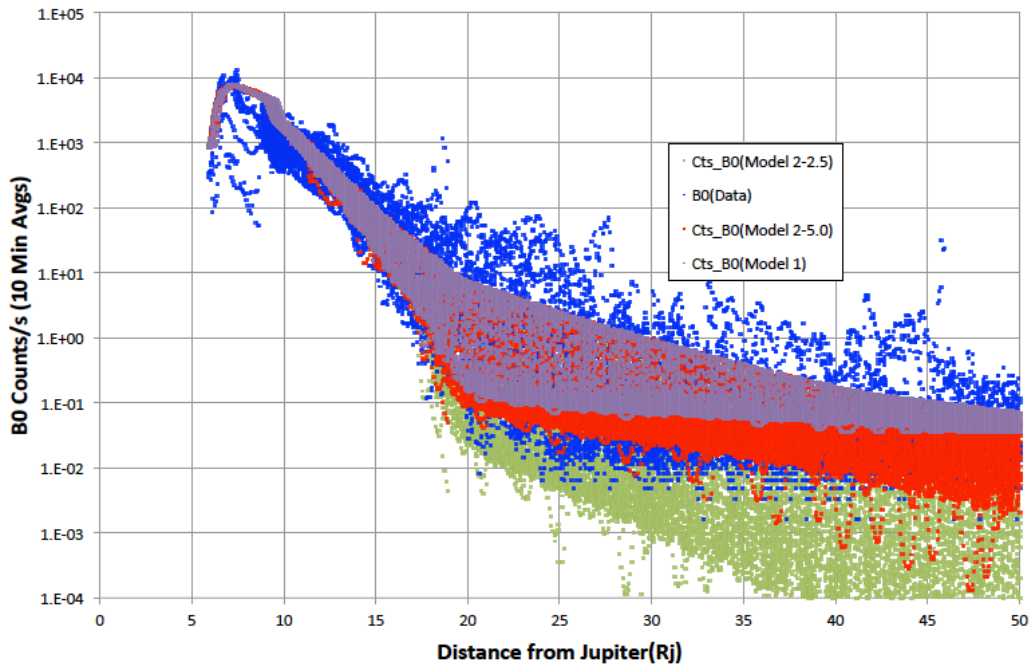
Figure 7. Estimates of the B0 channel count rates versus distance (Rj) compared with the measured B0 channel counts/second (10 minute averages). The data are plotted in blue and compared with the L-shell model assumption (purple), the scale height model in the outer magnetosphere (H = 2.5 Rj) in green, and the scale height model in the outer magnetosphere (H = 5.0 Rj) in red.
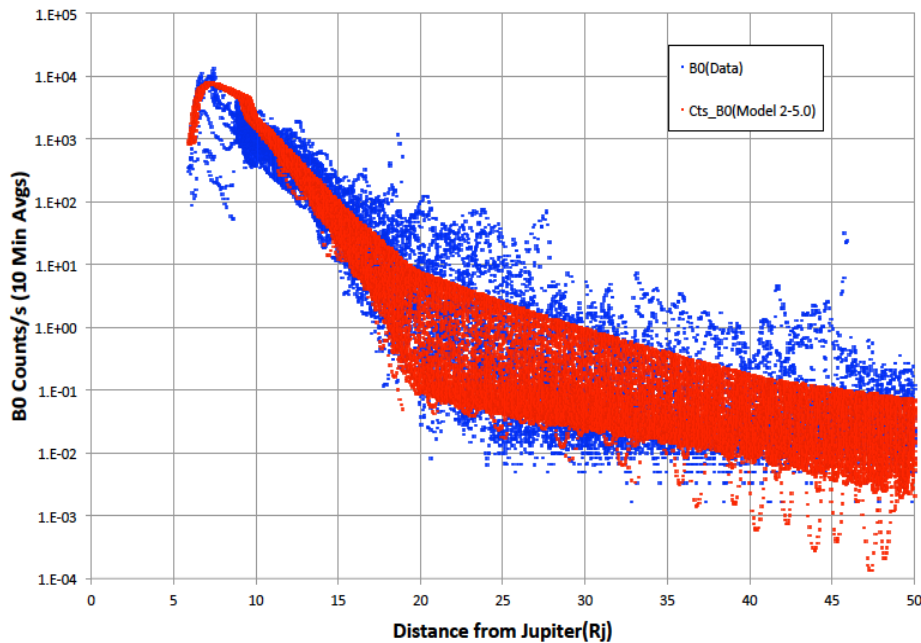
Figure 8. Estimates of the B0 channel count rates versus distance (Rj) for the scale height model in the outer magnetosphere with H = 5.0 Rj (red) compared with the measured B0 channel counts/second (blue).
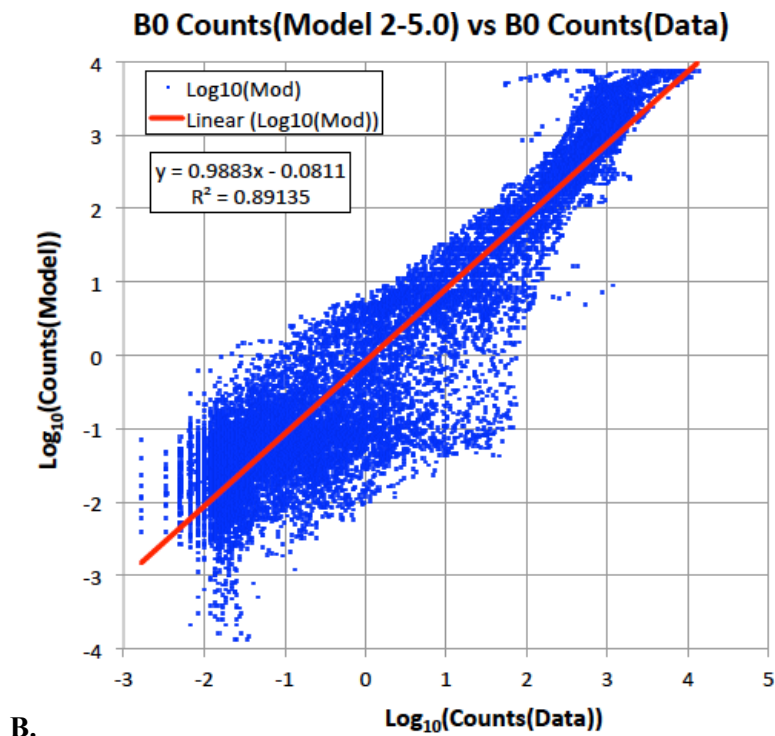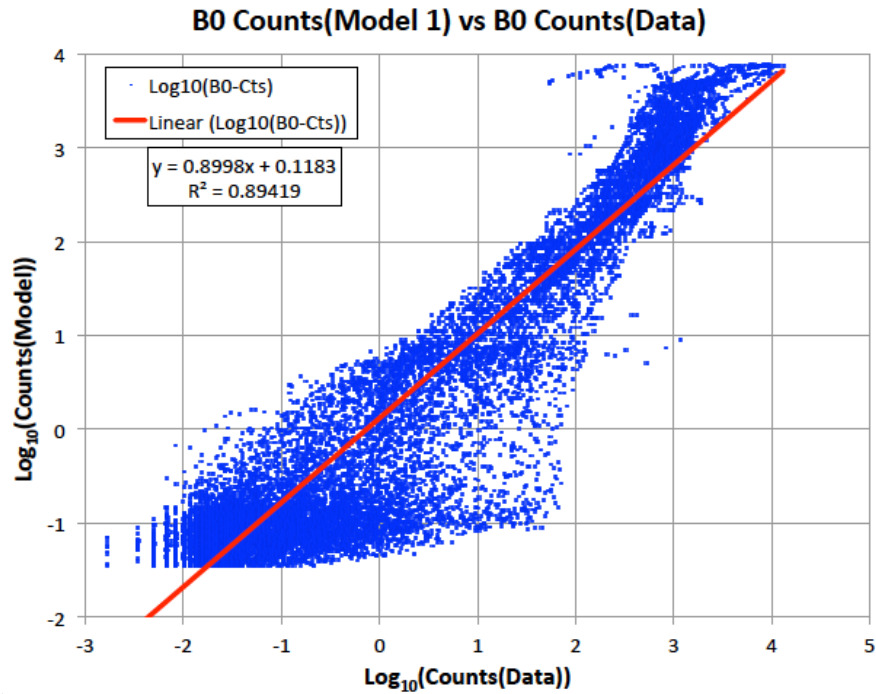
Figure 9. Predicted B0 channel count rates versus the observed B0 count rates for (A) the L-shell model and for (B) the scale height model in the outer magnetosphere with H=5.0. Linear regression fits to the log$_{10}$ of the count rates are included (Eqs. 7 and 8). (Note: the striations in the count data are digitization artifacts in the raw counts.)

 While the regression coefficients are essentially identical (both ~0.89), the equation for the scale height model for H = 5 Rj appears to give a better "1 to 1" relationship between the predicted and observed data.

That is, the constant relating the two logs is essentially 1 (0.9883) and the constant multiplier is ~0 (0.0811) so that it can be argued that Eq. 9 gives *B0(Model 2)~B0(Data)*.

As in our previous studies of the radiation environment at Jupiter (e.g., the EPD high energy electron data [Jun et al., 2005]), the data distribution may best be described in terms of a log–normal distribution (or probability density). That is:

$$\rho(r) = \frac{1}{\sigma\sqrt{2\pi}} e^{-\frac{1}{2}(\frac{r-\mu}{\sigma})^2} \tag{10}$$

where:

$\rho(r) = $ log–normal distribution function of variable r

$\mu = $ average value of r

$\sigma = $ standard deviation of r

$r = \log_{10}(J_{Data}/J_{Model})$

By the log–normal distribution, we mean that the $\log_{10}$ of the data follow a normal distribution. To validate the log–normal assumption, the ratio r computed for each 10-min B0 channel data point was summed over the data set, and then divided by number of points (17,252) to give an "average" value μ. The results are 0.083 for the μ or 1.21 for $10^{0.083}$. Ideally this "average," μ, should be 0 (or 1 for 10^μ) but the model fit is not exact and the data are only approximated by a log–normal distribution. Similarly, the "standard deviation" σ of the $\log_{10}$ of the points for this "average" was also computed. This quantity is of interest as a measure of the uncertainty of the proton radiation environment as estimated by the model for the B0 channel energy range. The value for σ is 0.62 corresponding to a factor of $10^{0.62} = $ ~4.1—that is, the proton model is typically within a factor of 4 of the actual data. This can be compared to a factor of 1.5 to 3.5 for the high energy electron component [Jun et al., 2005].

3.   Heavy Ion Models

This section discusses the extension of the JPL model to other high energy ions and compares the model with data from the Galileo HIC instrument [Garrett et al., 2011b] to demonstrate the extended range of the model. In addition to hydrogen (H), the APL EPD study [Mauk et al., 2004] includes helium (He), oxygen (O), and sulfur (S) (Fig. 4). The latter three ion species have been incorporated into the new model. Although they have not been "normalized" to the equator like the proton component (e.g., we do not have a reference channel like B0 for the protons), the same techniques were used to fold these new species into the model's flux computations. Selecting a specific species now generates differential and integral intensities as output based on Eq. 4 and Appendix A3, Table A2, from the APL study. Representative spectra from that paper were reproduced in Fig. 4. Similar contour plots to those of the protons in Fig. 6 are presented in Fig. 10 (here the Z_{map} version of the ion model was employed using H = 2.5 Rj to illustrate how the fluxes would fall off much faster than in Fig. 6).

From 1995 to 2003, the Galileo Heavy Ion Counter (HIC) [Garrard et al., 1992; Garrett et al., 2011b] monitored the high energy (~6 to >200 MeV/nuc), heavy ion ($_6$C to $_{28}$Ni) fluxes at Jupiter and returned data for all but 2 of the 35 orbits of the Jupiter system. HIC was based on a re-engineered Voyager Cosmic Ray System instrument and was flown in part to gain a better understanding of the heavy ion radiation environment at Jupiter than that given by the brief flyby missions of Pioneer and Voyager. These spacecraft found oxygen and sulfur to be the primary constituents of the heavy-ion environment at Jupiter—HIC added carbon, believed to be of solar origin, to the list. While the sulfur is primarily Io-genic, the oxygen is from mixed sources being either of solar origin or from sputtering off the icy moons of Jupiter. In any case, these oxygen and sulfur components allow linking of the HIC data with the EPD oxygen and sulfur data to provide heavy-ion spectra over a wide range of energies and to test whether the spectra "match up."

Based on the HIC measurements, a quantitative model of the jovian equatorial heavy ion radiation environment has been developed [Garrett et al., 2011b]. The model defines the fluxes for oxygen (5-40 MeV/nuc), carbon (5–40 MeV/nuc), and sulfur (6.3–40 MeV/nuc) between ~5–25 Rj. Average differential flux spectra for these three components were developed in terms of energy for selected radial bins and in terms of energy and radial distance that allowed interpolation of the fluxes at intermediate values for the two variables. In particular, to convert the fluxes into a simple engineering model capable of interpolation, the values were averaged over energy for selected Rj ranges and over Rj at specific energies. These gave two flux curves, one in energy and one, $J_{0j}(R)$, in radial distance. The product of these two curves at each energy and Rj were fit to a dual power law curve in energy. Assuming the two variables, energy (E) and radial distance (R), were independent, the flux at the discrete radial distances were multiplied by an energy spectrum of the form [Garrett et al., 2011b]:

$$JHIC_j(E,R) = JHIC_{0j}(R) \cdot E^{-A_j} \left(1 + \frac{E}{E_{0j}}\right)^{-B_j} \tag{11}$$

where:

$JHIC_j(E,R)$ = Flux in units of (n$^{\#}$/cm^2 s sr MeV/nuc)

$JHIC_{0j}(R)$ = Flux variation function in R; see [Garrett et al., 2011b]

E = Ion energy in MeV/nuc

R = Radial value (in jovian radii) at the average of the specified interval

A_j, B_j = Fitted constants

E_{0j} = Fitted constant (in MeV/nuc)

j = subscript indicating species; carbon, oxygen, or sulfur
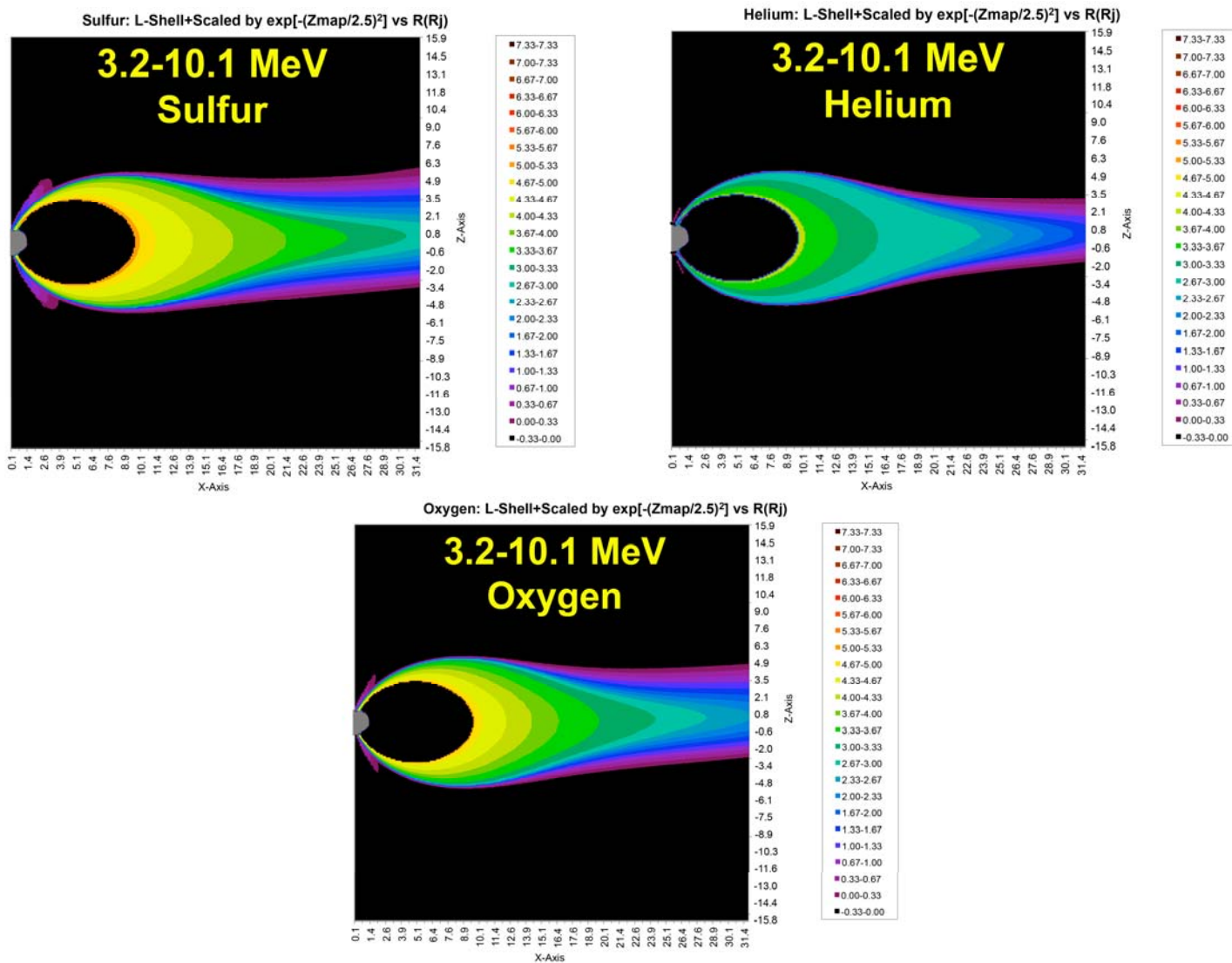
Figure 10. Comparison between the Sulfur, Helium, and Oxygen ion species for E>3.2 MeV for the new (DG2) GIRE2 ion model. The contours plotted here assume that the equatorial fluxes are constant along a given L-shell inside 17 but fall off exponentially (see text) outside 22.5 L. The scale height is assumed to be 2.5 Rj. Note that the "black" fill inside L = 6 represents a lack of data, not an absence of flux.

As the model is based on averages over pitch angle from Galileo, which primarily orbits in the jovian equatorial plane, the model is considered valid for approximately ±2–3 Rj above or below that plane between 5–25 Rj (hence the choice of 2.5 Rj for the scale height variation in Fig. 10). The model defaults to the ambient galactic cosmic rays (GCR) levels for Carbon, Oxygen, and Sulfur values for fluxes below 10^{-6} (cm^2 s sr MeV/nuc)$^{-1}$ for carbon and oxygen and 10^{-8} (cm^2 s sr MeV/nuc)$^{-1}$ for sulfur. A sample plot of the oxygen data is provided in Fig. 11. Fig. 12 compares the HIC model flux predictions with the averaged data as functions of radial distance (Rj) from Jupiter and for selected HIC energy channels.
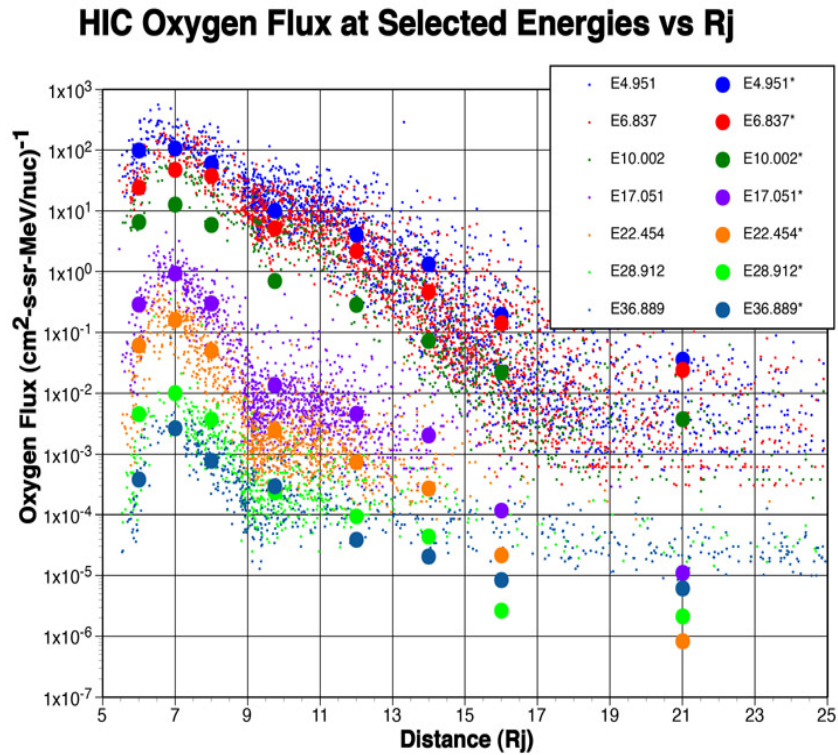
Figure 11. HIC oxygen fluxes [Garrett et al., 2011b] at selected energies versus radial distance. Also plotted are the average values for selected radial intervals that include the zero values (not visible in the plot as the vertical scale is logarithmic).
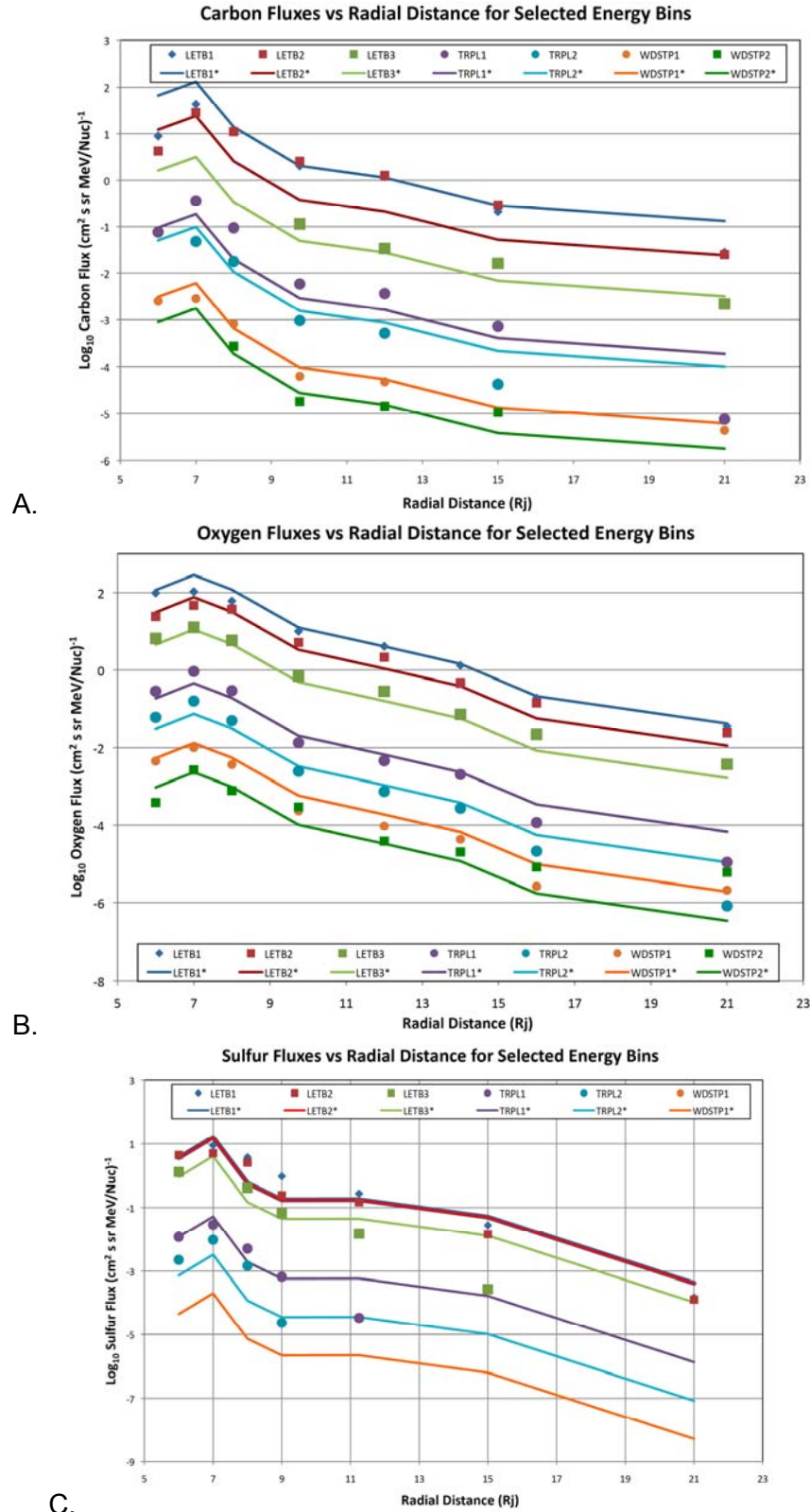
Figure 12. HIC average observations (points) compared to the HIC model fits for: (A) the carbon data; (B) the oxygen data; and (C) the sulfur data for selected HIC energy channels. Flux units are (cm²–s-sr-MeV/nuc)⁻¹ [Garrett et al., 2011b].
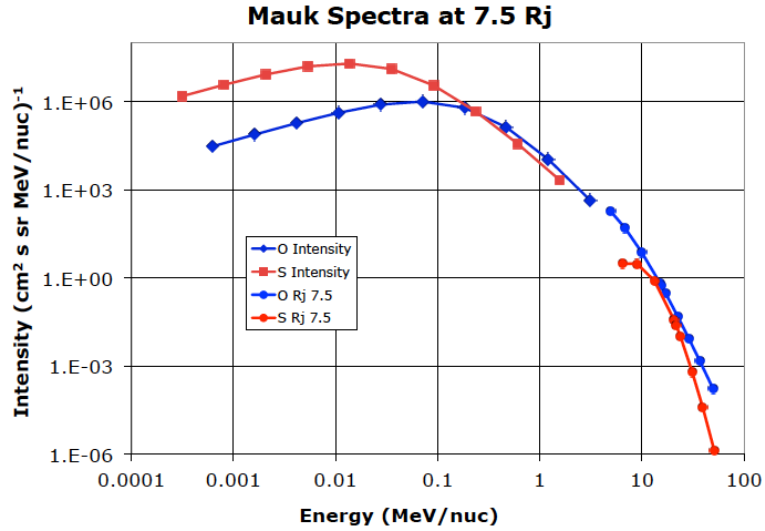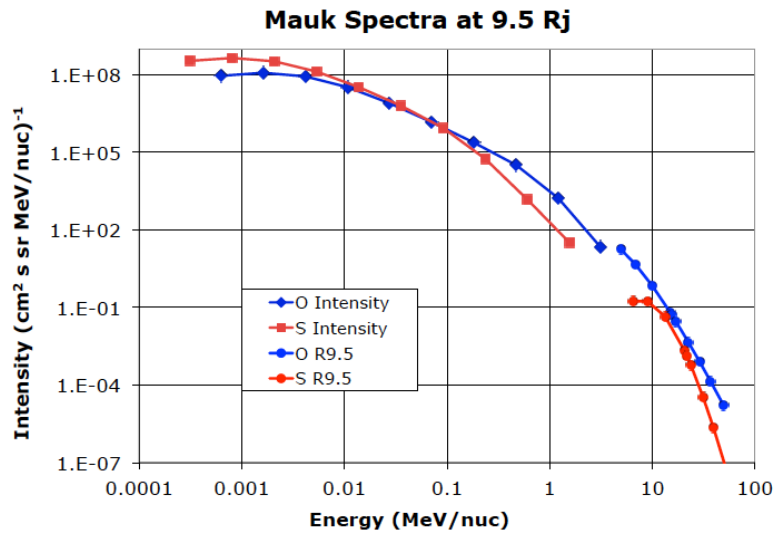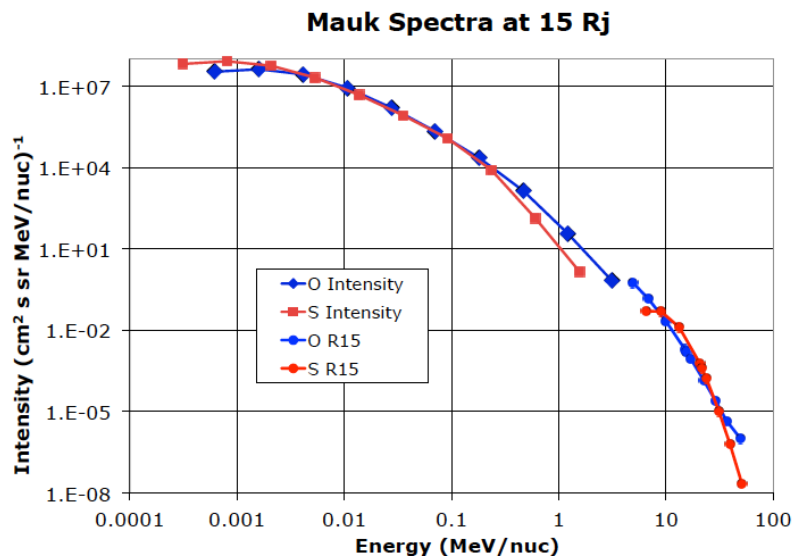
Figure 13. Comparisons between the modeled HIC data and the Galileo EPD spectra [Mauk et al., 2004] at (A) 7.5 R$_J$ (orbit JOI_1); (B) at 9.5 R$_J$ (orbit E6_Enc); and (C) at 15 R$_J$ (orbit G2_Enc).

As the EPD data [Mauk et al., 2004] provide oxygen and sulfur spectra up to several MeV/nuc (very near the lower limit of the HIC data), the HIC and EPD models can be compared to check their consistency over the extended energy range between 1 keV/nuc and 100 MeV/nuc. Fig. 13 compares three of the EPD reference ion spectra with the corresponding HIC estimates at the same distances. The comparisons, while not exact, imply rough agreement across the energy gap between the two very different models/instruments out to approximately 15 Rj (the models appear to diverge somewhat beyond that distance which is most likely due to "contamination" by the background GCR which begin to dominate the 10 MeV/nuc environment in the outer jovian magnetosphere as one moves away from Jupiter).

As an example of an application of the HIC model, Fig. 14 illustrates the HIC integral fluence spectrum (particles/cm^2) for a Europa Orbiter-like mission profile used in an early Europa orbit design study. As can be seen from Fig. 14, the ion fluences and their totals are close to or equal to the background GCR fluxes (e.g., the near-horizontal lines) past ~30 MeV/nuc. Note that the external GCR oxygen and carbon fluxes overlay each other. Sulfur dominates carbon at intermediate energies. The oxygen from the GCR background is labeled "OXYGEN CR," and the total of HIC oxygen and GCR oxygen is labeled "OXYGEN HIC+CR". Carbon, sulfur, and total fluences are labeled similarly. The line labeled "TOTAL HIC+CR" is the combination of Oxygen, Carbon, and Sulfur from the HIC model and the CRÈME 96 Cosmic Ray model.
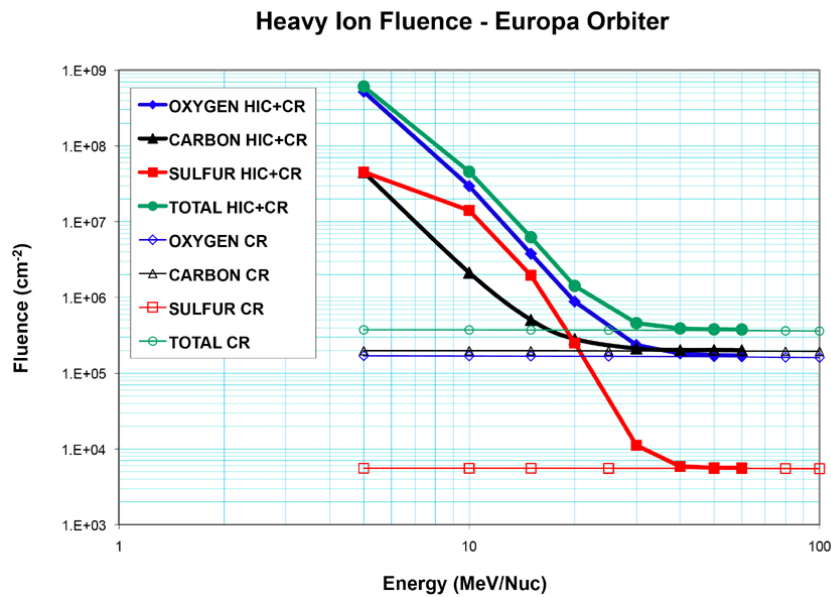
Figure 14. Galileo HIC model and GCR heavy ion fluences for a Europa Orbiter mission.

4.   Linking to the Jovian Plasma Environment

At the lower end of the energy spectrum are the DG1 plasma models. Divine and Garrett developed the DG1 jovian plasma models in the early 1980s [Divine and Garrett, 1983]. Since the original Pioneer and Voyager flybys that DG1 was based on, our understanding of those environments has been constantly improving. New measurements of that plasma environment from Galileo, Ulysses, Cassini, and Hubble have become available. Indeed, models of specific components of the Io plasma torus and plasma sheet by McNutt, Sittler, Bagenal, and colleagues [Bagenal and Delamere, 2011; 2014; Delamere et al., 2005; McNutt, 1980; McNutt et al., 1981; Sittler and Strobel, 1987; Smyth et al., 2011] and telescopic observations from the Shuttle of the jovian aurora [Ajello et al., 2001] are now available. Recent work [Garrett et al., 2015] incorporates these studies and new data into a revised plasma environment model. This update incorporated the cold and warm electron environments, the cold- and warm-ion environment, and the auroral fluxes throughout the jovian magnetosphere. To adequately describe these environments, the particle densities, temperatures, and, for the cold-ion components, their composition, ionization state, and drift velocities need to be defined. The particle distributions based on these parameters are usually defined in terms of either Maxwell-Boltzmann distributions:

$$f_i(v) = \frac{N_i}{\pi^{3/2} v_0^3} \exp(-v^2/v_0^2)$$

(12)

where:

$$v_0 = (2kT/m)^{1/2}$$

v = velocity relative to observation point (km/s); the convection velocity V_{cnvc}

can be incorporated here

N_i = number density (cm^{-3}) of species e^-, H^+, O^+, O^{++}, S^+, S^{++}, S^{+++}, Na^+

(i=0,1,2,..,7) or e^-(warm) and H^+(warm)

m = mass of species (g)

k = Boltzmann constant

T = temperature (K) of species

or the Kappa distribution:

$$f_\kappa(E) = N_\kappa (m_\kappa/2\pi E_0)^{3/2} \kappa^{-3/2} \frac{\Gamma(\kappa+1)}{\Gamma(\kappa-1/2)} \frac{1}{(1+E/\kappa E_0)^{\kappa+1}}$$

(13)

where:

$N_\square$ = Kappa number density (cm^{-3}) of species (e^- and H^+)

$m_\square$ = Kappa mass (g) of species (e^- and H^+)

$\kappa_\square$ = Kappa value

E_0 = Kappa temperature (or characteristic energy)

Typically a Maxwell-Boltzmann distribution with the convection velocity, V_{cnvc}, included in the velocity component is used to model the cold and warm plasmas—the convection velocity is approximately equal to the jovian rotation rate out to ~8 Rj but starts to lag it beyond that. Our studies have shown, however, that above ~1 keV and up to ~50–100 keV (where the proton and electron models overlap with the EPD data), a Kappa distribution is usually much better for fitting the particle distributions at Jupiter. In particular, as the high-energy electron and proton spectra tend to approach a power law variation between 1–6 MeV, the Kappa function can provide a continuous fit to the high-energy electron and proton spectra

between ~20 keV and ~1–6 MeV. Fig. 15 illustrates the model predictions for the warm proton Maxwell-Boltzmann distributions between 1–50 keV. Also shown are the high energy proton spectra predicted by the new proton model at the same equatorial distances—superimposed on the warm and high-energy proton spectra are corresponding Kappa distribution fits to the two spectra. The latter were fit to the warm Maxwell-Boltzmann distributions and the corresponding high-energy spectra to provide a continuous spectral fit between 1–10 keV and ~1–6 MeV and eliminate the artificial discontinuities in energy in this important region for spacecraft charging. Even though the warm proton component of the plasma model is not as well define as other parts of our model [Garrett et al., 2015], the Kappa fits indeed appear to closely approximate the Maxwell-Boltzmann distributions below 1–10 keV and join continuously onto the high energy fluxes for the new proton model between 600 keV and 6 MeV (the range over which the two proton populations were "smoothed").

The new high energy proton model allows us to extend the range of the Kappa distribution fits for the protons throughout most of the jovian magnetosphere. Therefore, based on the preceding assumptions, contour plots at 110°W have been generated that illustrate the basic structure of the proton plasma environment around Jupiter in terms of a Kappa distribution for energies between ~1 keV and ~600 keV. Fig. 16 illustrates these contours for the warm-proton Kappa components (see Eq. 13 for a definition of the Kappa constant).
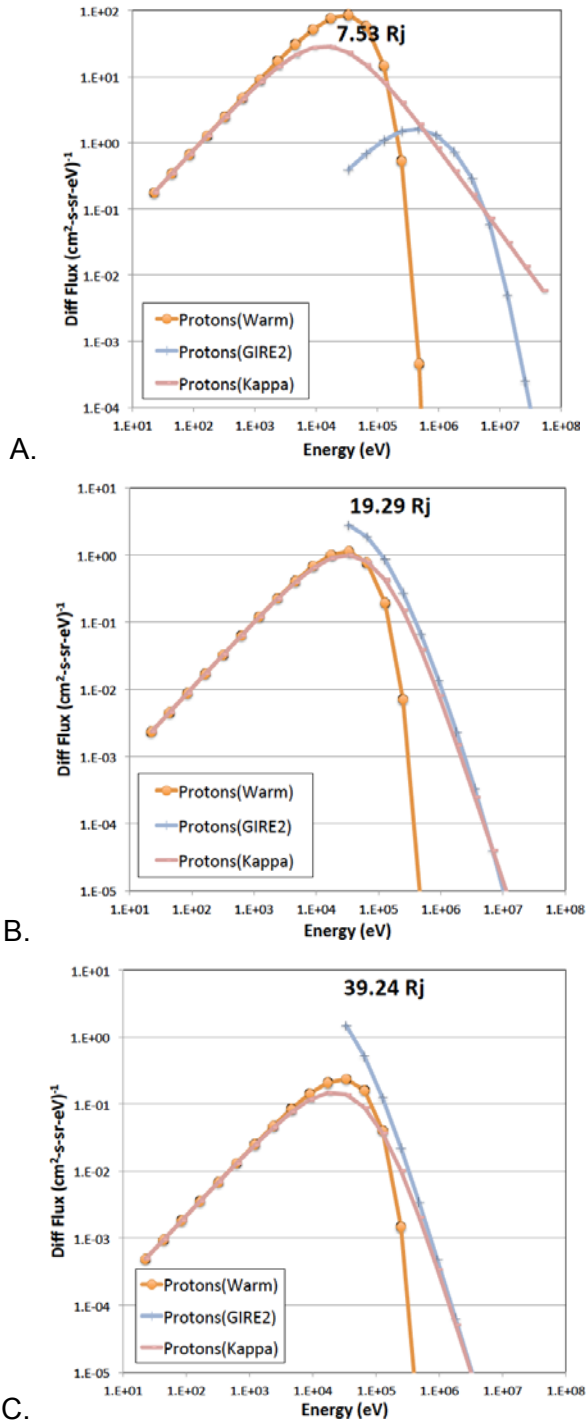
Figure 15. Warm Maxwell-Boltzmann plasma distributions for protons and estimates of the E>50 keV protons for the new model. To smoothly fit the warm populations onto the high energy components, proton spectra between 10 eV and 6 MeV were fit to the two distributions using a Kappa distribution. (Note: The new proton model should be assumed above ~1 MeV.)
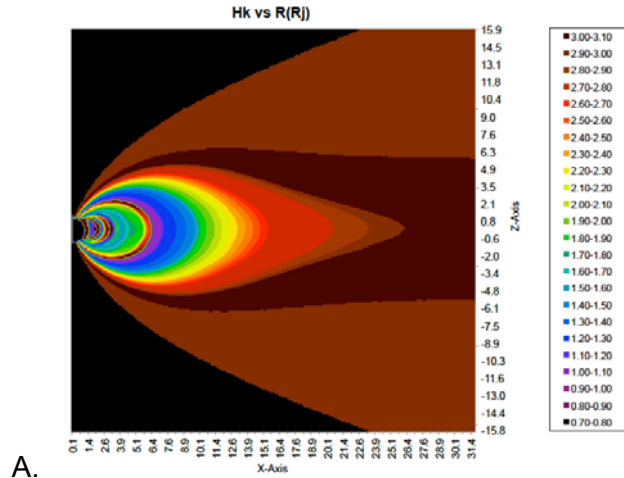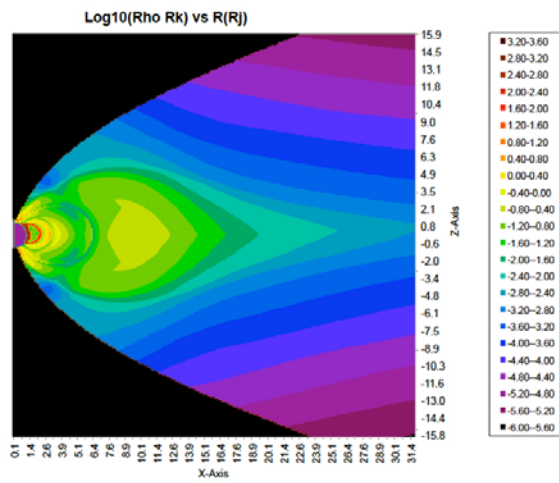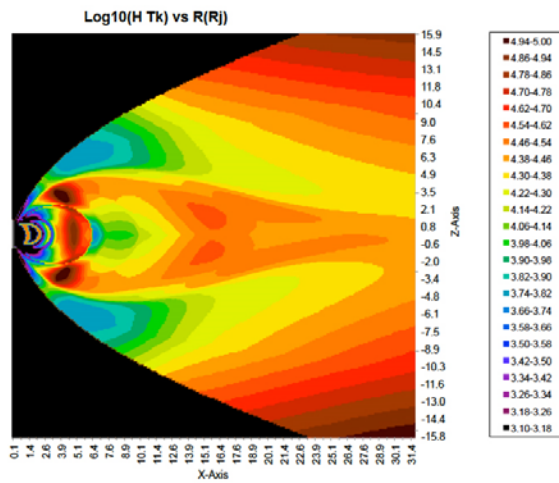
Figure 16. Meridional contour plots of the three proton Kappa parameters (Kappa value, density, and temperature) as fit to the DG2 plasma model and the new high energy proton model. The energy range of applicability is from ~1 keV up to ~600 keV.

5.   Conclusions

To conclude, the original Divine model [*Divine and Garrett,* 1983], DG1, has been the basis of many design studies of the effects of the jovian plasma and radiation environments on spacecraft systems. The original environments included in the model were the low energy electrons and ions, warm electrons and ions, and high energy electrons and protons covering most of the jovian magnetosphere inside ~50 Rj—an exception being the high energy protons which were limited to L<12. While proving to be an excellent tool over the last 30 years, the model has become "dated" as new data have become available from Galileo and other sources. Indeed, our interpretations of the original data have also evolved. This paper describes an important improvement to the original DG1. In particular, the proton environment from ~50 keV to ~50 MeV has been updated between ~6 Rj to ~50 Rj. In addition to hydrogen, helium, oxygen, and sulfur ions were added over this same range. The model now allows for studies of the effects of the energetic ions on solar arrays and, when linked at the low energy end, surface charging, or, when linked with the HIC ion model, the effects of single event upsets. The original model has become an even more useful tool for designing and evaluating missions to Jupiter, and it is hoped that it will be used extensively in the design of the next Jupiter mission, Europa.

6. References

Ajello, J. M., D. E. Shemansky, W. R. Pryor, A. I. Stewart, K. E. Simmons, T. Majeed, J. H. Waite, G. R. Gladstone, and D. Grodent (2001), "Spectroscopic Evidence for High-Altitude Aurora at Jupiter from Galileo Extreme Ultraviolet Spectrometer and Hopkins Ultraviolet Telescope Observations," *Icarus*, *152*, 151–171.

Bagenal, F., and P. A. Delamere (2011), "Flow of mass and energy in the magnetospheres of Jupiter and Saturn," *J. Geophys. Res.*, *116* (A05209), doi:10.1029/2010JA016294.

Bagenal, F., and P. A. Delamere (2014), LASP Galileo PLS Data Analysis, http://lasp.colorado.edu/

Connerney, J. E. P., M. H. Acuna, N. F. Ness, and T. Satoh (1998), "New models of Jupiter's magnetic field constrained by the Io flux tube footprint," *J. Geophys. Res.*, *103*(A6), 11,929–911,940.

Delamere, P. A., F. Bagenal, and A. Steffl (2005), "Radial variations in the Io plasma torus during the Cassini era," *J. Geophys. Res.*, *110* (A12223), doi:10.1029/2005JA011251.

Divine, T. N., and H. B. Garrett (1983), "Charged particle distributions in Jupiter's magnetosphere," *J. Geophys. Res.*, *88* (Sept. 9), 6889–6903.

Garrard, T. L., N. Gehrels, and E. C. Stone (1992), "The Galileo Heavy Element Monitor," *Space Sci. Rev.*, *60*, 305–315.

Garrett, H. B., R. W. Evans, and W. Kim (2015), "EHM Jovian Plasma for Charging Evaluation Task Final Report," *IOM-5130-15-001* (internal document), Jet Propulsion Laboratory, California Institute of Technology, Pasadena, CA.

Garrett, H. B., I. Jun, J. M. Ratliff, R. W. Evans, G. A. Clough, and R. W. McEntire (2003), *Galileo Interim Radiation Electron Model*, JPL Publication 03-006, 72 pp, Jet Propulsion Laboratory, California Institute of Technology, Pasadena, CA, Pasadena, CA.

Garrett, H. B., M. Kokorowski, I. Jun, and R. W. Evans (2012b), *Galileo Interim Radiation Electron Model Update—2012*, JPL Publication 12-9, Jet Propulsion Laboratory, California Institute of Technology, Pasadena, CA.

Garrett, H. B., M. Kokorowski, S. Kang, R. W. Evans, and C. M. S. Cohen (2011b), *The Jovian Equatorial Heavy Ion Radiation Environment*, JPL Publication 11-16, Jet Propulsion Laboratory, California Institute of Technology, Pasadena, CA.

Garrett, H. B., S. M. Levin, S. J. Bolton, R. W. Evans, and B. Bhattacharya (2005), "A revised model of Jupiter's inner electron belts: Updating the Divine radiation model," *Geophys. Res. Lett.*, *32 (4)*(L04104), doi:10.1029/2004GL021986.

Hill, T. W., and F. C. Michel (1976), "Heavy ions from the Galilean satellites and the centrifugal distortion of the Jovian magnetosphere," *J. Geophys. Res.*, *81*, doi:10.1029/JA081i025p04561.

Jun, I., H. B. Garrett, R. Swimm, R. W. Evans, and G. A. Clough (2005), "Statistics of the variations of the high-energy electron population between 7 and 28 jovian radii as measured by the Galileo spacecraft," *Icarus*, *178*, 386–394, doi:10.1016/j.icarus.2005.01.022.

Jun, I., J. M. Ratliff, H. B. Garrett, and R. W. McEntire (2002), "Monte Carlo simulations of the Galileo energetic particle detector," *Nucl. Instr. and Meth., A*, *490*, 465–475.

Khurana, K. K., and H. K. Schwarzl (2005), Global structure of Jupiter's magnetospheric current sheet, *J. Geophys. Res.*, *110*(A07227), doi:10.1029/2004JA010757.

Martinez Sierra, L. M., H. B. Garrett, and I. Jun (2015), "Radiation Environment Model of Protons and Heavier Ions at Jupiter," paper presented at AIAA Space 2015, American Institute of Aeronautics and Astronautics, Pasadena, CA, September 1, 2015.

Mauk, B. H., D. G. Mitchell, R. W. McEntire, C. P. Paranicas, E. C. Roelof, D. J. Williams, S. M. Krimigis, and A. Lagg (2004), "Energetic ion characteristics and neutral gas interactions in Jupiter's magnetosphere," *J. Geophys. Res.*, *109*(A09S12), 24, doi:10.1029/2003JA010270.

McNutt, R. L., Jr. (1980), *The Dynamics of the Low Energy Plasma in the Jovian Magnetosphere*, Ph.D. thesis, Massachusetts Institute of Technology, Cambridge, MA.

McNutt, R. L., Jr., J. W. Belcher, and H. S. Bridge (1981), "Positive ion observations in the middle magnetosphere of Jupiter," *J. Geophys. Res.*, *86*, 8319–8342.

Pelowitz, D. B. (2011), *MCNPX TM User's Manual*, Version 2.7.0, *LLC, la-cp-11-00438 ed.*, Los Alamos National Laboratory, Los Alamos, NM.

Sittler, E. C., Jr., and D. F. Strobel (1987), "Io plasma torus electrons: Voyager 1," *J. Geophys. Res.*, *92* (A6), 5741–5762.

Smyth, W. H., C. A. Peterson, and M. L. Marconi (2011), "A consistent understanding of the ribbon structure for the Io plasma torus at the Voyager 1, 1991 ground-based, and Galileo J0 epochs," *J. Geophys. Res.*, *116* (A07205), doi:10.1029/2010JA016094.

Williams, D. J., R. W. McEntire, S. Jaskulek, and B. Wilken (1992), "The Galileo Energetic Particles Detector", *Space Sci. Rev.*, 60, 385–412.

7.   Appendix A1. Data Sources for DG1

Table A1. Data sources for the original Divine and Garrett model [Divine and Garrett, 1983].

Instrument	Data Type
	Pioneers 10 and 11
Helium vector magnetometer (HVM)	vector magnetic field
Flux gate magnetometer (FGM)	vector magnetic field
Plasma analyzer (PA)	electrons and protons, 0.1 to 4.8 keV
Geiger tube telescope (GTT)	electrons >0.06, 0.55, 5, 21, 31 MeV
	protons 0.61-3.41 MeV
Trapped radiation detector	electrons >0.16, 0.26, 0.46, 5,
(TRD)	8, 12, 35 MeV
	protons >80 MeV
Low-energy telescope (LET)	protons 1.2–2.15 and 14.8-
	21.2 MeV
Electron current detector (ECD)	electrons >3.4 MeV
Fission cell (FI)	protons >35 MeV
	Voyagers 1 and 2
Flux gate magnetometer (MAG)	vector magnetic field
Planetary radio astronomy (PRA)	electric vector, 1.2 kHz to
	40.5 MHz
Plasma wave (PWS)	10 Hz to 56 kHz
Plasma science (PLS)	electrons 10–6000 eV
	ions 10–6000 V
Low-energy charged particle (LECP)	electrons >15 keV
	ions >30 keV
Cosmic ray telescope (CRT)	electrons 3–110 MeV
	ions l–500 MeV/nucleon
	Earth
Radio telescopes	UHF intensity and polarization

8. Appendix A2. APL Spectra Fits

Table A2. Energetic ion spectral parameters at various positions within Jupiter's magnetosphere (ion energies 50 KeV to 50 MeV) [Mauk et al., 2004]. Constants are defined in Eq. 4. Sample spectral plots are presented in Fig. 4.

	Orbit	JOI-5	JOI-4	JOI-3	JOI-2	JOI-1	E6_Mequ	E4_Enc	E6_Enc	G2_Enc	C3_Aur	G8_PS/A	G2_PS	G7_PS
	Year	1995	1995	1995	1995	1995	1997	1996	1997	1996	1996	1997	1996	1997
	Day	341	341	341	341	341	51	354	51	250	310	126	255	89
	Time, UT	1736	1654	1639	1609	1539	2136	2167	1643	1836	706	1443	247	1924
	R, RJ	6	6.52	6.71	7.1	7.48	9.13	9.49	9.51	15.15	19.28	25.16	39.25	46.3
	lat-SysIII, deg	-0.23	-0.82	-1	-1.34	-1.64	-0.17	-0.198	-0.497	0.122	-0.286	-0.849	-0.33	-0.046
	long-SysIII, deg	-90.7	-110	-117	-131	-146	119	167	-30	145	142	124	127	146
	LT, deg	-4	-10.4	-12.4	-16.1	-19.4	40	72	12.6	-19.2	-46	-90	178	-108.5
	maglat, deg	3.45	5.55	6.2	7.2	7.75	1.02	7.7	-6.41	5.41	4.5	1.24	2.14	5.3
	E-Max, MeV H,	50	50	50	50	50	50	50	50	50	50,6,18,21	32,6,9,10	3,4,2,10	3,4,2,10
	He, O, S													
H	C	2.96E+05	2.00E+07	7.99E+06	3.51E+06	8.94E+09	8.82E+07	2.79E+06	4.05E+07	6.84E+10	1.63E+09	1.36E+10	5.78E+08	3.36E+08
	Kt, KeV	75.4	1384.9	1179.5	849.5	281.9	120.8	4.5	30.9	31.8	18.7	10.1	6.6	10.6
	gam	1.35	1.111	0.978	0.859	2.027	1.566	1.213	1.617	2.884	2.581	3.129	3.139	3.105
	et, KeV	10,430	2383	2383	2383	6965	5719	6880	5660	10,955	5000			
	gam2	3.404	2.783	2.773	3.096	2.815	2.813	4.177	2.534	0.435	1.416			
O	C	6.78E+10	2.86E+14	1.29E+14	1.93E+14	6.90E+14	7.44E+08	9.19E+06	1.30E+08	2.35E+08	3.34E+08	2.21E+13	3.07E+12	9.15E+10
	Kt, KeV	340.4	1797.2	1674	1198.4	952.1	130	8.6	17.2	16.1	20.8	42.6	27.4	16.6
	gam	2.829	3.179	3.064	3.122	3.307	2.093	1.647	1.997	2.343	2.496	4.048	4.299	3.844
	et, KeV	14,750	8512	8512	8512	8535	15,290	10,838	14,455	6833	6836			
	gam2	-0.5	0.802	0.994	1.152	0.815	3.111	2.793	2.945	1.989	1.454			
S	C	1.06E+10	4.21E+11	1.62E+11	1.49E+11	3.34E+11	1.49E+09	1.42E+07	1.60E+08	4.81E+07	5.71E+07	1.15E+12	4.83E+13	8.76E+09
	Kt, KeV	184	725.3	654.5	439.8	323	120	8.6	17.2	16.1	20.8	42.6	34.8	16.6
	gam	2.678	2.585	2.446	2.435	2.541	2.093	1.599	1.912	2.03	2.144	3.543	4.435	3.352
	et, KeV	24,802	8408	8408	8408	7912	5696	5700	4948	6588	5004			
	gam2	1.025	0.479	0.653	0.844	0.785	2.154	2.616	2.213	2.818	3.132			
He	C						1.55E+06	8.02E+04	7.73E+05	3.45E+09	1.80E+08	1.38E+09	4.89E+09	2.73E+09
	Kt, KeV						120.8	4.5	30.9	31.8	18.7	11.8	6	21
	gam						1.566	1.213	1.617	2.884	2.581	3.171	3.106	3.707
	et, KeV						5719	6880	5660					
	gam2						2.813	4.177	2.534					

9.   Appendix A3. Acronyms and Abbreviations

APL   Johns Hopkins University Applied Physics Laboratory

B0   Galileo EPD particle channel for protons between 3.2 and 10.1 MeV

CMS   Composition Measurement System

CR   count rate

CTS   counts per second

DG1   Divine and Garrett 1983 model

DG2   Galileo Interim Radiation Electron Model (2012)

EPD   Energetic Particle Detector

ET   Solar System Barycentric Ephemeris Time

GCR   Galactic cosmic rays

GIRE   Galileo Interim Radiation Electron model (2003)

GIRE2   Galileo Interim Radiation Electron model, Version 2 (also referred to as DG2)

HIC   (Galileo) Heavy Ion Counter experiment

JHU   Johns Hopkins University

JOI   Jupiter Orbit Insertion

LEMMS   Low-Energy Magnetospheric Measurement System

MAG   (Galileo) Magnetometer

MCNP   Monte Carlo N-Particle Transfer Code

MCNPX   Monte Carlo N-Particle eXtended Code

NAIF   (NASA) Navigation and Ancillary Information Facility

PDS   Planetary Data System

RBEHS   R(adius) B(field) E(PD) H(IC) S(tarscanner) data base

Rj   Jupiter radius, 71,400 km

UT   Universal Time